An All-Day Attitude Sensor Integrating Stars and Sun Measurement Based on Extended Pixel Response of CMOS APS Imager

Hongjing Cao, Haiyang Zhan, Jingdong Li, Qilong Rao, Fei Xing, and Zheng You

***Abstract*— For celestial measurement, it is difficult to enable a single optical system to image and measure both stars and the sun due to the vastly different light intensity of targets and the limited response capability of the image sensor pixel. Here, we develop an all-day optical attitude sensor integrating stars and the sun measurement based on the extended pixel response model of the CMOS active-pixel sensor (APS) imager. For extremely large light intensity, we extend the conventional pixel response model to the oversaturated stage where the pixel values reverse and drop below the saturation value. Based on this, the integration of the star sensor and the sun sensor is realized. The pixels image the starry sky with linear response, and make use of the oversaturation response to image the sun and obtain a black spot on the bright background. This principle enables the capability of all-day high-precision attitude measurement using a single miniaturized sensor. An integrated optical attitude sensor is designed and manufactured. Ground-based observation results show that the orientation accuracy from sun measurement is better than 9" (3σ), and the attitude accuracy from star measurement is better than 5" (3σ) for pointing and 11" (3σ) for rolling. The sensor can be applied to high-precision all-day navigation systems for miniaturized spacecraft and aircraft.**

***Index Terms*— Attitude measurement, optical instrumentations, optical measurement, space instrumentations.**

I. Introduction

NAVIGATION is an indispensable key technology in various fields such as aviation, aerospace, and marine [1], [2], [3], [4]. Celestial navigation is an important way to realize automated navigation by detecting the celestial bodies with known accurate spatial positions [5]. It does not rely on any external man-made facilities, and therefore, is not susceptible to spoofing attacks and signal blockage and jamming [6], [7], [8]. In addition, since the positions of celestial bodies are absolute at a given moment, celestial navigation has no cumulative error so it is of high value in long-time-duration missions [1], [9]. Unlike visual navigation, celestial navigation does not depend on the ground features of the working environment, and it does not need to map the complex environment [10], [11]. Nowadays, automated celestial navigation is combined with other navigation methods to improve navigation accuracy, increase security, and provide an effective means of checking for major errors in special scenarios, especially in important military strategic occasions [12], [13]. With the increasing application of small spacecraft and aircraft, and the increasingly complex tasks, the all-day celestial navigation system becomes requisite, and the requirements for its miniaturization are also raised.

Automatic celestial navigation is mainly realized through optical attitude sensors, including star sensors and sun sensors. Star sensors can achieve high-precision celestial navigation by extracting and identifying bright star spots in digital images [14], [15], [16], [17]. However, the insufficient ability of a star sensor to observe stars in daylight limits its use as an all-day navigation system [18]. The background light intensity of star images in daylight is millions of times that of the dark sky, resulting in stars being difficult to detect as weak targets. In order to improve the signal-to-noise ratio, high-precision all-day star sensors usually have a large mass and volume [19], which are not suitable for small spacecraft and aircraft. Sun sensors can achieve celestial navigation by extracting the image of the sun. Liu et al. achieved daytime navigation through a hemispherical sun sensor array. The sun vector measurement accuracy was $0.2^\circ \times 0.1^\circ$ [20], [21], [22]. However, the sun sensor is always not sensitive to weak light and may not respond when imaging starry sky, which can only be used during the day when the sun is in the field of view (FOV) and cannot realize all-day navigation by itself. One solution to achieve all-day celestial navigation is to combine multiple types of sensors such as sun sensors or polarized light sensors [23], [24], [25] and star sensors. Guo et al. used nine polarized light sensors distributed in a hemisphere to assist with starlight and inertial information and developed an integrated navigation system that can work normally even when only one star is observed during the day. The simulation results showed that it realized an accuracy of 0.02° [26]. The existing combination solutions work with

Manuscript received 17 November 2022; revised 10 February 2023; accepted 12 March 2023. Date of publication 7 April 2023; date of current version 19 April 2023. This work was supported in part by the National Natural Science Foundation of China under Grant 51827806 and Grant U21A6003, in part by the National Key Research and Development Program of China under Grant 2016YFB0501201, and in part by the Xplorer Prize funded by the Tencent Foundation. The Associate Editor coordinating the review process was Dr. Yang Bai. *(Corresponding author: Fei Xing.)*

Hongjing Cao, Haiyang Zhan, Jingdong Li, Fei Xing, and Zheng You are with the Beijing Advanced Innovation Center for Integrated Circuits, Department of Precision Instrument, and the State Key Laboratory of Precision Measurement Technology and Instruments, Tsinghua University, Beijing 100084, China (e-mail: caohj20@mails.tsinghua.edu.cn; hbyszhy@163.com; 18811395682@163.com; xingfei@mail.tsinghua.edu.cn; yz-dpi@mail.tsinghua.edu.cn).

Qilong Rao is with the Shanghai Institute of Satellite Engineering, Shanghai 201109, China (e-mail: mrrao2561@126.com).

Digital Object Identifier 10.1109/TIM.2023.3265092

TABLE I
CHARACTERISTICS OF PREVIOUS CELESTIAL NAVIGATION SENSORS AND THE INTEGRATED ALL-DAY SENSOR

Techniques	Characteristics	Accuracy
Common star sensors [14]-[17]	Night navigation only	high accuracy of several arcseconds
All-day star sensors [19], [35]	All-day navigation, big size and mass	high accuracy of several arcseconds
Hemispherical sun sensor array [21]	Daytime navigation only	0.2°× 0.1°
Polarized light sensor [26]	Assisting with the star sensor to achieve daytime navigation	0.02°
Sun sensor with black sun effect [33]	Daytime navigation only	0.013°
The proposed integrated all-day sensor	All-day navigation with a single optical system	Daytime 9" (3σ), night 5" (3σ) for pointing and 11" (3σ) for rolling

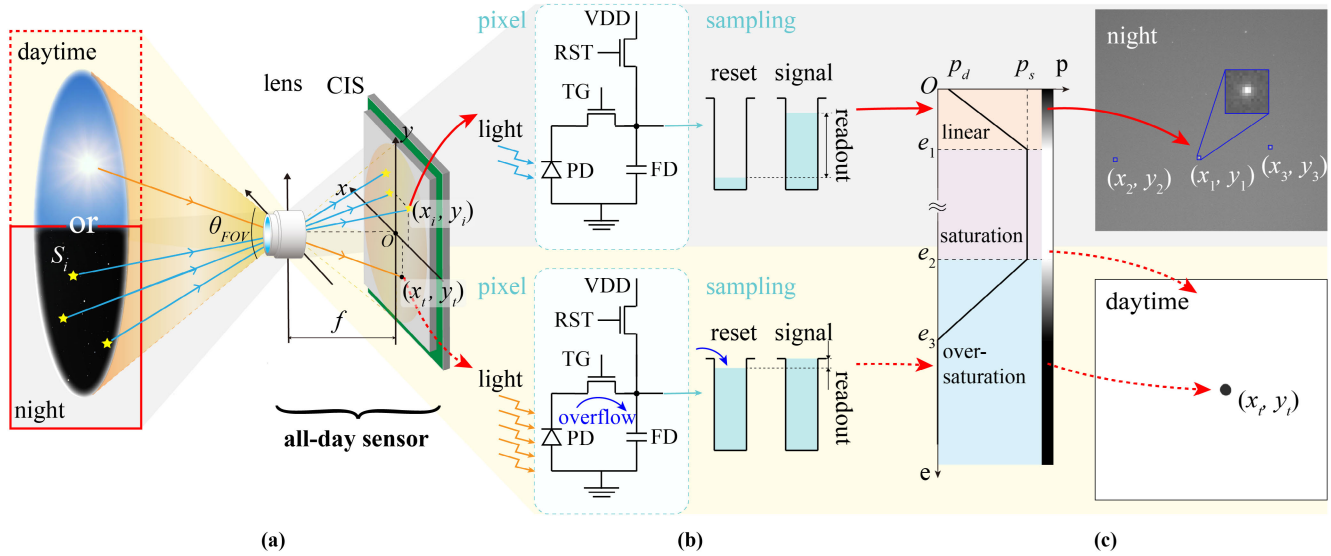

Fig. 1. Principle of integrated all-day optical attitude sensor. The part with yellow shading in the figure corresponds to the work state as a sun sensor during the day, and that with gray shading corresponds to the work state as a star sensor at night. (a) Measurement model of the integrated all-day optical attitude sensor during the daytime and night, respectively. (b) Pixel circuit and signal sampling of the pixels for star imaging and black sun imaging on the CIS. Extremely strong sunlight causes the overflow (bluish violet arrow) to raise the reset level and mistake the pixel readout value. (c) Extended CIS pixel response model and imaging of the all-day optical attitude sensor. Working as a star sensor at night, the acquired image is multiple bright spots on a dark background with pixels responding in the linear stage. Working as a sun sensor during the daytime, the image is a black spot on a bright background with pixels responding in the oversaturation stage. In this sun image, the background pixels are all saturated.

large instrument mass and volume, but limited orientation measurement accuracy.

The difference in intensity between the sun and stars is huge, which can span a super-wide range of more than 10^{11} times. Therefore, it is difficult to realize the integration of the star sensor and the sun sensor with one optical system [27], [28], [29]. In addition, for conventional camera-based sun sensors, the extremely strong light leads to a blooming phenomenon or other artifacts on the image [30]. The circular sun image is extracted through image processing techniques such as the circular Hough transform [31]. The centering accuracy of the sun image is limited, which in turn affects the orientation measurement accuracy. Recently, artifacts have also been utilized to improve sun extraction accuracy. Cheng et al. [22] made use of the blooming phenomenon of the charge coupled device (CCD) image sensor to extract both the circular image of the sun and the blooming line to estimate the position of the sun's center. Besides, a phenomenon called the black sun effect has also been discovered and applied to sun sensors [32]. This phenomenon occurs because the extremely strong sunlight causes the signal readout (RO) of the image sensor to be abnormal, and the image of the sun is reversed from a bright spot to a black spot. Saleem et al. [33] made use of the black sun effect to improve the image processing method, so as to reduce the adverse influence of complex sun artifacts, achieving an accuracy of 0.013° under static conditions. They also developed a sun-tracking CMOS image sensor (CIS) with a black-sun readout scheme [34]. Actually, we find the image sensor with the black sun effect still has the ability to image weak light targets normally, and it opens up the possibility for the integration of stars and the sun measurement. In addition, based on the detailed analysis of the cause of the black sun

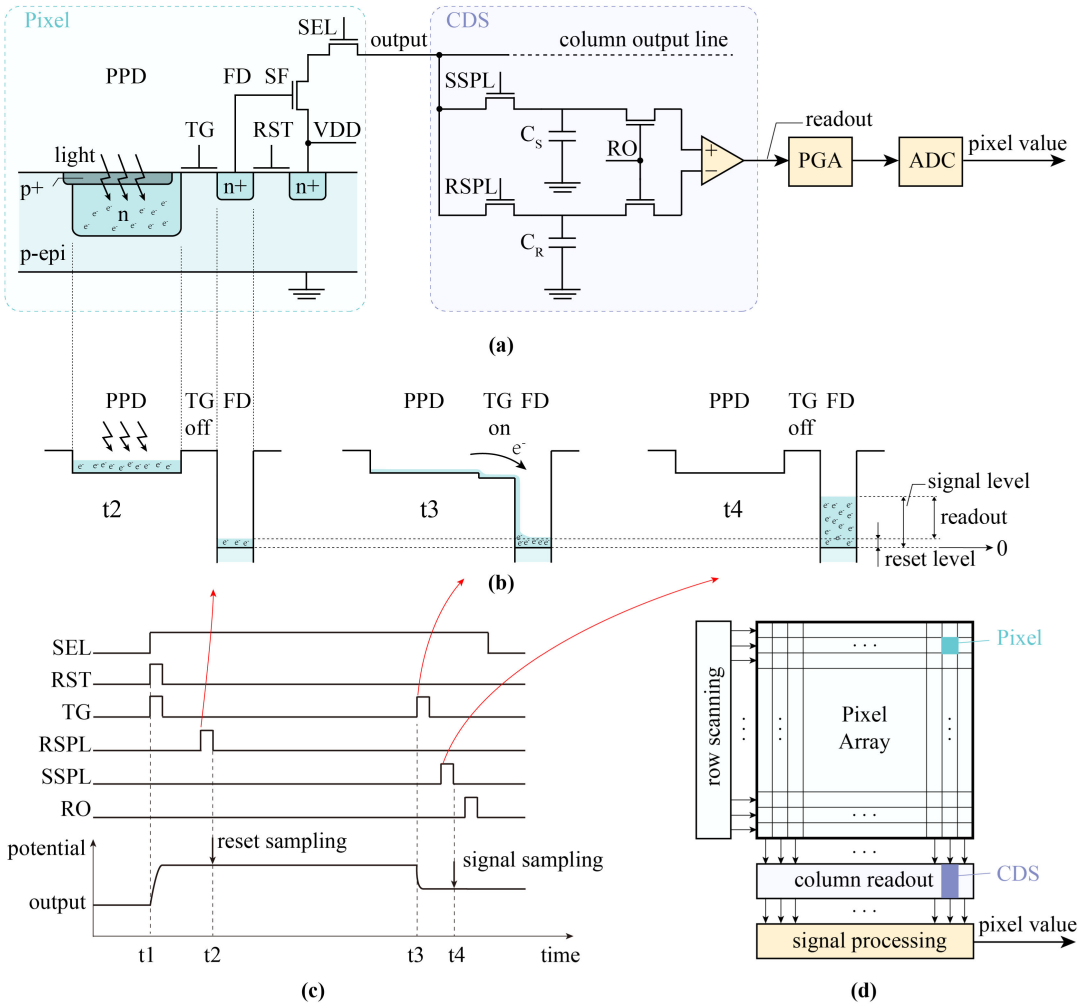

Fig. 2. Schematic of the signal generation and readout of the CIS with 4T-PPD pixels under normal intensity illumination. (a) General schematic circuit diagram of the pixel structure, column CDS readout circuit, and subsequent signal processing. The pixel structure and CDS readout circuit are respectively in the blue frame and the purple frame. (b) Potential profile of the pixel reset sampling, charge transferring, and signal sampling. (c) Complete timing sequence and output potential of a pixel in a single exposure cycle. (d) CIS simplified structure diagram.

effect, the accuracy of the sun sensor using this effect can be further improved through appropriate design and optimization of the optical system.

In this article, we develop a high-precision miniaturized all-day optical attitude sensor integrating stars and the sun measurement based on the extended pixel response model of the CIS. We explain in detail the cause of the black sun effect at the pixel circuit level of the CIS, extend the pixel response model, and achieve the integrated design of the star sensor and the sun sensor on this basis (see Fig. 1). First, we analyze the principle of signal generation and readout of the CIS with four-transistor pinned photodiode (4T-PPD) pixels under normal and extremely strong light. Based on the correlated double sampling (CDS), we propose an extended response model of the CIS pixel, which covers pixel response to weak and very strong light in linear and oversaturation stages, respectively. Moreover, the integration of the star sensor and the sun sensor is realized, and an all-day optical attitude sensor is designed and manufactured. Ground-based observation experiments of stars and the sun have verified it effectiveness and accuracy. The work significantly improves the accuracy of the sun measurement, combining the high-precision stars measurement meanwhile, and provides an approach for all-day celestial navigation system miniaturization. The characteristics of previous celestial navigation sensors and the integrated all-day sensor are shown in the Table I.

II. Extended Pixel Response Model of CIS

A. Signal Generation and Readout Under Normal Illumination

The research is based on the CIS with 4T-PPD pixels that applies CDS for pixel signal readout. The general schematic circuit diagram is shown in Fig. 2(a), which illustrates the pixel structure, column CDS readout circuit, and subsequent signal processing. The signal processing mainly includes signal amplification through the programmable gain amplifier (PGA) and analog-to-digital conversion (ADC). This section analyzes the signal generation and readout under normal light intensity, that is, when the generated photoelectrons do not exceed the full well capacity (FWC) of the pixel.

A pixel consists of a pinned photodiode (PPD), a floating diffusion (FD), and four transistors that include a reset transistor (RST), a transfer gate (TG), a source follower (SF), and

a select transistor (SEL) [36], [37]. The PPD receives light to generate photoelectrons, which are collected and accumulated in the formed potential well as signal charges. The TG forms a potential barrier when turned off. If the charge in the PPD does not exceed the FWC, the potential barrier can prevent the charges from reaching the FD. Only a very small amount of charges leak to the FD due to the thermionic emission [38]. When the TG is on, the charges can be transferred to the FD, and the charge in FD is converted into voltage by SF [39]. The potential change of FD is given by

$$\Delta V = \frac{Q_{\mathrm{FD}}}{C_{\mathrm{FD}}} \tag{1}$$

where Q_{FD} is the amount of charge in FD, and C_{FD} is the equivalent charge-to-voltage conversion capacitance.

In order to eliminate the fixed pattern noise (FPN) of the pixel, the CDS readout method is adopted. Two sets of sampling-hold (S/H) circuits sample and hold the reset level (the amount of charges) and the signal level respectively, and then the two sampling values enter the differential amplifier for subtraction operation. Fig. 2(b) illustrates the potential profile of the pixel reset sampling, charge transferring, and signal sampling respectively.

The complete timing sequence and output potential of a pixel in a single exposure cycle are shown in Fig. 2(c). First, RST and TG are turned on to reset the PPD and FD to the high potential (t1). Subsequently, TG is turned off, and RSPL is on for reset sampling (t2). Under normal intensity light, the reset level is low and represents the reset noise.

During exposure, photoelectrons are generated and accumulated in PPD and the potential of PPD drops. When TG is on again, the signal charges are transferred to and maintained in FD (t3), and then SSPL is on for signal sampling (t4). At this moment, the charge in the FD is the sum of the signal charge and reset noise charge. Finally, the reset level and signal level enter the differential amplifier through RO to calculate the FPN-eliminated low-noise readout value

$$\text{readout} = \text{signal level-reset level}. \tag{2}$$

SEL remains on during the process, indicating that this row is selected. The pixel exposure time lasts from the end of the reset to the beginning of the charge transfer.

All pixels in the same row perform the above process at the same time. Signals in the same column are readout by the same output line and CDS circuit. The readout value of each pixel is converted into the pixel value, a digital signal, through the subsequent signal processing [see Fig. 2(d)].

B. Signal Readout Under Extremely Strong Light

Charge collection and accumulation in the PPD are the basis for subsequent signal output and readout. However, the FWC of the pixel limits the number of electrons that the potential well of PPD can store. It determines the maximum output of the pixel, and in turn, determines the imaging dynamic range and the maximum signal-to-noise ratio of the CIS.

The height of the potential barrier formed by TG is one of the important factors affecting the value of the FWC [40].

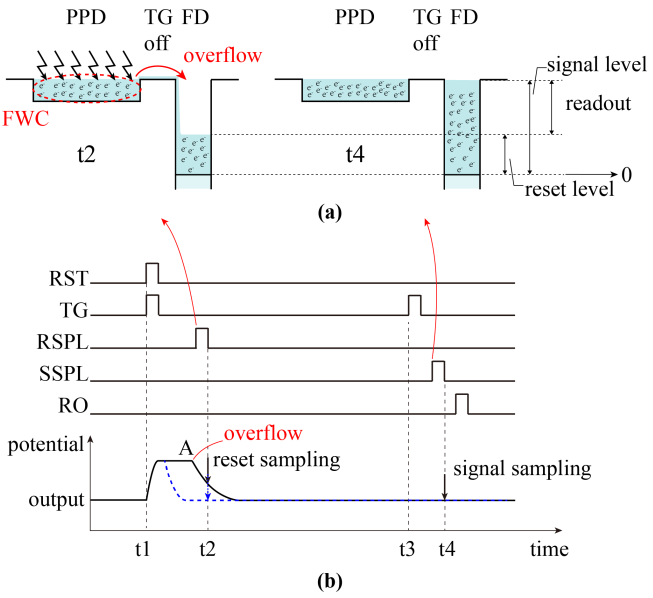

Fig. 3. Schematic of the signal readout of the 4T-PPD pixel under extremely strong light. (a) Potential profile of the pixel reset sampling and signal sampling when the amount of charges exceeds FWC and charges overflow to FD. (b) Timing sequence and output potential of a pixel at the corresponding time. The blue dotted line indicates the case of much stronger light than the black solid line, and the readout value has dropped to zero.

During the charge accumulation process of PPD, when the charge largely exceeds the FWC, the potential barrier formed by TG will be insufficient to prevent the charges from reaching the FD. If there is no effective compensation measure to discharge the excess charges of the pixel, the charges will overflow to the FD or surrounding pixels. The actual charge overflow is related to the design and manufacturing of the pixel structure [41]. Overflow to surroundings may aggravate crosstalk between CIS pixels, and cause unexpected phenomena such as blooming.

When the incident light is extremely strong, the charge overflow to the FD may affect the reset level sampling (see Fig. 3). Due to the extremely high light intensity, a large number of generated photoelectrons quickly reach the FWC after the reset process, and then overflow to the FD. The time at which overflow occurs is marked as point A in Fig. 3(b). When the reset sampling is performed at t2, the reset level is actually higher than the expected value, while the signal level reaches the saturation level [see Fig. 3(a)]. In this case, the readout value obtained by subtracting the two [see (2)] will be less than the saturation value, and the readout value cannot truly indicate the light intensity. That is to say, when the light intensity reaches a certain level, the readout value will no longer increase with the increase of light intensity, but will decrease, and even decrease to zero [bluish violet dotted line in Fig. 3(b)], which depends on the amount of charges overflowing to the FD when the reset sampling is performed. Obviously, the greater the light intensity is, the faster the overflow will occur.

C. Extended CIS Pixel Response Model

Based on the pixel response characteristics developed in the European Machine Vision Association (EMVA) 1288 standard

[42] and the analysis of the signal readout in Sections II-A and -B, we extend the CIS pixel response model to the full intensity range. This response model describes the relationship between the final pixel value and the number of electrons induced by full-range light intensity throughout an exposure cycle of a pixel (including crosstalk electrons from other pixels and excluding electrons overflowing to other pixels). It should be noted that the model meets the linear assumptions put forward by EMVA 1288 standard model before the pixel value reaches saturation

$$\mu_y = K(\mu_e + \mu_d) \tag{3}$$

where μ_y is the mean digital signal, μ_e is the mean of accumulated electrons increasing with light intensity, μ_d is the mean of electrons present without light, which results in the dark signal, and K is an overall system gain with a unit of digits per electrons. For an n-bit ADC, the pixel value ranges from 0 to 2^n-1, and the maximum value corresponds to the pixel saturation capacity $\mu_{e.\text{sat}}$, which does not reach the FWC in general cases [42]. The pixel can no longer linearly respond for μ_e larger than $\mu_{e.\text{sat}}$, and the pixel enters the saturation state.

This article further describes the situation when the light intensity continues to increase. As described in Section II-B, when the number of photoelectrons in PPD exceeds the FWC, they may overflow to the FD. If the light is extremely strong, photoelectrons are accumulated rapidly in PPD and quickly exceed the FWC before the reset sampling. A large number of excess photoelectrons overflow to the FD and affect the reset sampling, causing the reset level to be high and the pixel value to decrease. The pixel value response is reversed, which stage is defined as oversaturation here. In real scenarios, strong light sources such as the sun and lasers may cause this to happen. The number of electrons making the pixel value begin to reverse is denoted as $\mu_{e.\text{rev}}$. With the light intensity continuing to increase, the pixel value will be reduced to zero at $\mu_{e.\text{zero}}$ electrons. Note that the values of $\mu_{e.\text{rev}}$ and $\mu_{e.\text{zero}}$ in our extended model refer to the total number of electrons accumulated over the entire exposure cycle of the pixel, instead of the electrons accumulated during the very short time before the reset sampling instant which increase the reset level. These two values can be estimated as

$$\mu_{e.\text{rev}} = \text{FWC} \cdot \frac{t_3}{t_2} \cdot \mathcal{F} \tag{4}$$

$$\mu_{e.\text{zero}} = 2\text{FWC} \cdot \frac{t_3}{t_2} \cdot \mathcal{F} \tag{5}$$

where t_2 and t_3 are the reset sampling time and the exposure time in one exposure cycle respectively (see Fig. 3). $\mathcal{F}$ is the function indicating the effect of crosstalk between pixels and is affected by multiple variables, which can be ignored in the rough calculation.

In summary, the extended CIS pixel response model includes three stages: linearity, saturation, and oversaturation according to the number of pixel electrons (see Fig. 4). We assume that the reset level increases uniformly as the total number of photoelectrons of the pixel increases between $\mu_{e.\text{rev}}$ and $\mu_{e.\text{zero}}$, and (3) is extended to

$$\mu_y = \begin{cases} K(\mu_e + \mu_d) & 0 \le \mu_e \le \mu_{e.\text{sat}} \\ 2^n - 1 & \mu_{e.\text{sat}} \le \mu_e \le \mu_{e.\text{rev}} \\ \max\left(\dfrac{K(\mu_{e.\text{sat}} + \mu_d)}{\mu_{e.\text{zero}} - \mu_{e.\text{rev}}}(-\mu_e + \mu_{e.\text{zero}}), 0\right) & \mu_e \ge \mu_{e.\text{rev}} \end{cases}. \tag{6}$$

The model greatly extends the response range of the CIS pixel, which can perceive a super large range of light intensity. As analyzed above, the extended model is suitable for CIS pixels using the CDS method with no compensations for charge overflow. When the strong light causes the reset sampling value to be higher than the true level, the pixel can respond in the oversaturation stage.

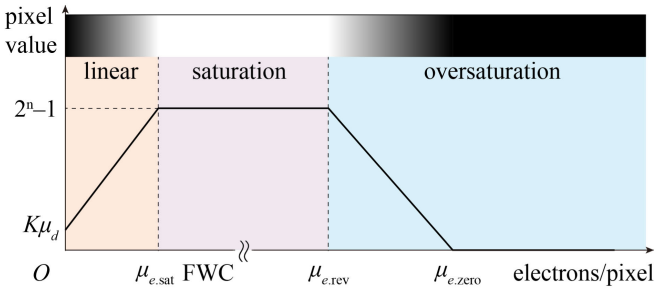

(a)

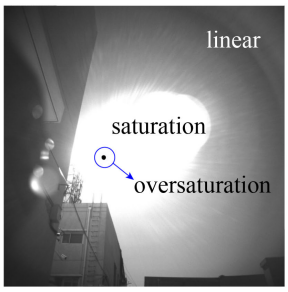

(b)

Fig. 4. Extended CIS pixel response model. (a) Extended CIS pixel response characteristic curve including linearity, saturation, and oversaturation stages. The upper part illustrates that as the number of pixel electrons increases, the image grayscale representing the pixel value changes. (b) Grayscale image containing all three response stages. The extremely strong light that causes oversaturation comes from the sun. The high-value pixels around the oversaturated response area are in the saturation response state.

III. Integrated All-Day Optical Attitude Sensor

A. Integration Principle of Star Sensor and Sun Sensor

Optical attitude sensors rely on imaging celestial bodies such as stars and the sun. The light emitted by the celestial bodies reaches the photosensitive area of the image sensor through the optical system, and the images of the celestial bodies are output. The attitude can be further solved by extracting the centers of the celestial bodies in the images. Clear imaging and easy extraction of celestial targets are crucial for improving the measurement accuracy of attitude sensors.

The aperture and focal length of the optical system determine the number of photons that can reach the photosensitive

area and the FOV of the attitude sensor, which in turn determine the pixel values of the output image and the imaging effect of celestial bodies. The design idea of conventional star sensors and sun sensors is to make the CIS pixels respond linearly when imaging the targets. In this case, due to the huge difference between the light intensity of stars and the sun, the sun sensors and the star sensors need to use very different optical systems.

Since the starlight is relatively weak, star sensors usually have a relatively large aperture and a long exposure time to obtain star images containing multiple bright spots on the dark background. In addition, the optical systems of star sensors have a relatively long focal length to improve measurement accuracy with a low requirement of FOV.

The measurement model is illustrated in Fig. 1(a). For star sensors, the principal point of the image plane is $O(x_0, y_0)$, and the focal length of the optical system is f. When imaging stars, each star spot is extracted with a position of (x_i, y_i), and the corresponding star vector in the sensor coordinate system is expressed as

$$S_i = \frac{1}{\sqrt{(x_i - x_0)^2 + (y_i - y_0)^2 + f^2}} \begin{bmatrix} x_i - x_0 \\ y_i - y_0 \\ -f \end{bmatrix}. \tag{7}$$

Through subsequent star map recognition and calculation, the absolute attitude of the sensor in the inertial coordinate system can be determined.

The sunlight is extremely strong compared to the starlight. Conventional camera-based sun sensors always use an optical system with a small aperture and short focal length to avoid saturation of the whole image or artifacts like blooming that affect the extraction of the sun image and expand the FOV. Sun sensors may also be equipped with neutral filters to reduce light transmission.

For sun sensors, the solar incidence angle can be calculated by extracting the centroid of the sun spot (x_t, y_t). The two-axis solar incidence angle in the sensor coordinate system can be expressed as

$$\begin{cases} \alpha = \arctan\left(\dfrac{x_t - x_0}{f}\right) \\ \beta = \arctan\left(\dfrac{y_t - y_0}{f}\right) \end{cases}. \tag{8}$$

Actually, based on the extended response model, sunlight can excite enough electrons to make the CIS pixels reach oversaturation with a well-designed optical system. In this case, the image of the sun is a black spot on the bright background, and this is called the black sun phenomenon, just as the sun image in Fig. 4(b). When employing the black sun phenomenon to observe the sun, the centroid of the black sun spot is extracted and the angle is calculated according to (8).

If a single imaging system can respectively utilize the linear and oversaturation stages of CIS pixels to image stars and the sun clearly, it is possible to realize the integration of a star sensor and a sun sensor. Such an integrated optical attitude sensor can work as a sun sensor during the day and as a star sensor at night to achieve all-day attitude measurement or celestial navigation.

Obviously, determining the positions of the star spots and the center of the sun is significant for the accuracy of attitude measurement. The black sun spot appears in the center with the highest energy. Compared with conventional sun imaging, it has the characteristics of a small spot and simple background, making it easier to extract, and in turn improving the accuracy of orientation measurement and reducing calculation difficulty without a complex extraction algorithm.

B. Design Principle of the All-Day Attitude Sensor

In order for the integrated all-day attitude sensor to realize the functions of both the star sensor and the sun sensor, the imaging and measurement requirements of the two need to be considered in the optical system design.

First, the FOV and accuracy of the sun and stars measurement need to be considered comprehensively. According to the measurement model of the optical attitude sensor, the focal length affects the theoretical accuracy δ (single star pointing accuracy) and the FOV (θ_{FOV}) of the sensor

$$\delta = \arctan\left(\frac{a \cdot l_{\mathrm{pix}}}{f}\right) \tag{9}$$

$$\theta_{\mathrm{FOV}} = 2\arctan\left(\frac{L_{\mathrm{area}}}{2f}\right) \tag{10}$$

where a is the centroid extraction accuracy of the star image in pixels, and it can be taken as 0.1, achieving sub-pixel accuracy, and l_{pix} is the pixel size of CIS, L_{area} is the width of the photosensitive area. The rolling accuracy can be approximately estimated as $(4f/L_{\mathrm{area}}) \cdot \delta$. For measurements with M identifying stars, the accuracy in (9) should be divided by $\sqrt{M}$, which will be affected by θ_{FOV}.

When l_{pix} and L_{area} are determined, there is a fundamental tradeoff between the theoretical measurement accuracy and the FOV. If the FOV of the sensor is enlarged, the measurement accuracy will be degraded accordingly. For celestial navigation during the daytime, the sun is the only observation target, so it is necessary to expand the FOV. It should be as large as possible while ensuring high accuracy, and a CIS with a large photosensitive area can be selected.

Then, imaging of the celestial targets is considered, which is the basis for attitude measurement and calculation. Section II has analyzed the relationship between the response pixel value and the number of photoelectrons. Fundamentally, the number of photoelectrons is determined by the radiation of the light source, CIS spectral response, quantum efficiency, exposure time, and lens aperture [43]. For the sun and stars of spectral class G2, an optical lens with an aperture diameter of D will cause the image sensor to generate photoelectrons

$$N = \int_{\lambda_1}^{\lambda_2} \frac{I(\lambda, T) \cdot \eta(\lambda)}{hc/\lambda} d\lambda \cdot 2.512^{0-Mv} \cdot t_{\mathrm{exp}} \cdot \frac{\pi D^2}{4} \tag{11}$$

where $I(\lambda, T)$ is the radiation from a blackbody at a given wavelength and temperature, $\eta(\lambda)$ is the quantum efficiency of the CIS at wavelength λ, h is the Planck constant, c is the speed of light, and the optical system transmits wavelengths in the λ_1–λ_2 band. Mv is the apparent magnitude of the celestial target (that of the sun is –26.7), and t_{exp} is the exposure time of CIS. D and t_{exp} are the main design parameters.

Star sensors are adjusted to make most energy of a star point distributed within a $k \times k$ pixels window. The distribution of the image is usually assumed as following a 2-D Gaussian function. In the window of interest, the signal on the pixel with the lowest intensity should be effectively detected. Assuming that the center of the star spot coincides with the center of the window, the inequality should be satisfied

$$\frac{N_{\text{star}}}{2\pi\sigma_{\text{PSF}}^2} \cdot \exp\left(-\frac{\left(l_{\text{pix}} \cdot (k-1)/2\right)^2}{\sigma_{\text{PSF}}^2}\right) > \left(\frac{\sigma_{y.\text{dark}}}{K} + \frac{1}{2}\right) \quad (12)$$

where σ_{PSF} is the Gaussian radius, indicating the energy concentration of the star point spread function, $\sigma_{y.\text{dark}}$ is the standard deviation of dark noise, which can be estimated by CIS illumination experiments [42]. In order not to lose the effective signal, the number of electrons in the brightest pixel for a bright star should also be lower than $\mu_{e.\text{sat}}$, and in practical designs, we make it close to $\mu_{e.\text{sat}}$.

For black sun observation, due to the extremely large number of photoelectrons generated, complicated charge overflow exists inside and among pixels, and it is difficult to establish an exact model to describe the signal energy distribution on each pixel. Here, we simplify the pixel overflow process of photoelectrons and give the design principle of the integrated sensor for black sun observation, which is not completely exact but enough to work.

We assume that all photoelectrons induced by the sun are initially concentrated in m pixels corresponding to an angle of 0.53°, which is the viewing angular diameter of the sun as observed from the Earth. The basic design principle is that the number of photoelectrons generated by the image sensor is within the oversaturated response range of the pixel, that is

$$\mathcal{F} \cdot N_{\text{sun}}/m = \mathcal{F} \cdot N_{\text{sun}}/\left(\frac{f \tan 0.53^\circ}{l_{\text{pix}}}\right)^2 > \mu_{e.\text{rev}}. \quad (13)$$

In order to make the black sun spot more distinct from the bright background for easy extraction, $\mathcal{F} \cdot N_{\text{sun}}/m > \mu_{e.\text{zero}}$ should be guaranteed. According to (4), it can also be expressed as

$$N_{\text{sun}}/m > 2\text{FWC} \cdot \frac{t_3}{t_2}. \quad (14)$$

Besides the black sun observation principle, the design for the star observation should also be satisfied. Parameters such as exposure time and pixel gain can be adjusted according to the observation targets to improve the robustness of the optical system design for different working states. A design example is shown in Fig. 5. The typical sun sensors are with small focal length and aperture in order to enlarge the FOV and decrease the number of photoelectrons arriving at the imager. Besides, neutral filters are always equipped to avoid artifacts, and as a result, the number of photoelectrons generated by star imaging is extremely small. Relatively, the typical star sensors are with large focal length and aperture, so the theoretical measurement accuracy (single star) is high, and the FOV is small. The integrated all-day sensor determines the parameters within the range which satisfies the FOV of the sun measurement, accuracy, and the black sun and stars imaging.

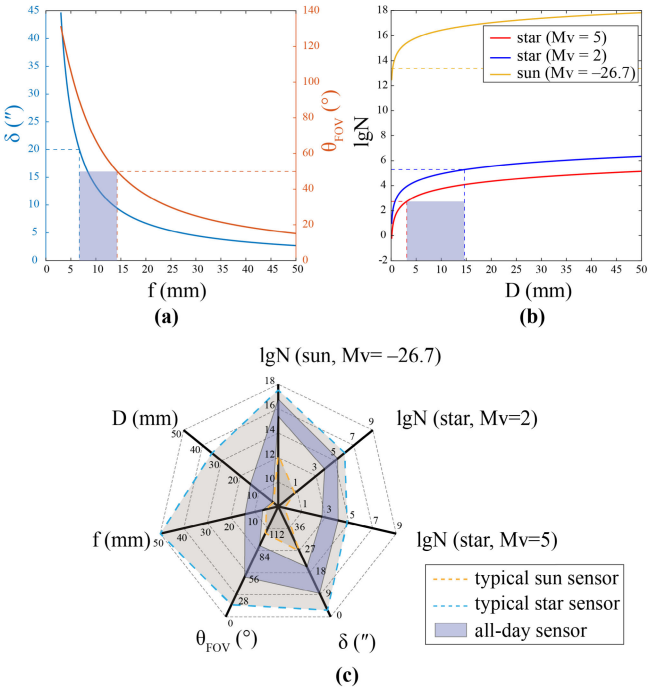

Fig. 5. All-day optical attitude sensor design principles. (a) Curve representing the FOV and theoretical precision of the optical sensor as a function of focal length. The purple area represents the selection range of the focal length of the all-day sensor considering the FOV and accuracy. (b) Curve representing the number of photoelectrons as a function of lens aperture. The curves of the sun and stars with different apparent magnitudes are represented separately. The number of photoelectrons is expressed by the common logarithm. The purple area represents the selection range of the lens aperture of the all-day sensor considering the effects of star and sun imaging. (c) Optical sensor parameter selection radar chart showing the design parameters of a typical star sensor and a sun sensor, and the parameter selection range of the all-day sensor. In fact, due to the larger FOV of the all-day sensor and the larger number of identified stars, the accuracy will not deteriorate too much compared to typical star sensors. The typical sun sensor calculation considers it adds a 0.1% neutral filter.

TABLE II
PARAMETERS OF THE INTEGRATED ALL-DAY OPTICAL ATTITUDE SENSOR

Characteristics	Performance
Focal Length	12.5mm
F Number	F/1.4
Pixel Size	6.5μm×6.5μm
Photosensitive Area Size	13.3mm×13.3mm
FOV	56°×56°
Theoretical Precision (single star)	10.7"
Size	33mm×33mm×37mm
Mass	60g
Power Consumption	1.5W for stars, 0.6W for the sun

IV. EXPERIMENTS AND RESULTS

According to the design principle described in Section III-B, a lens with a focal length of 12.5 mm and F/1.4, and a CIS with a pixel size of 6.5 × 6.5 μm and a photosensitive area size of 13.3 × 13.3 mm are selected. The composed integrated optical attitude sensor has an FOV of

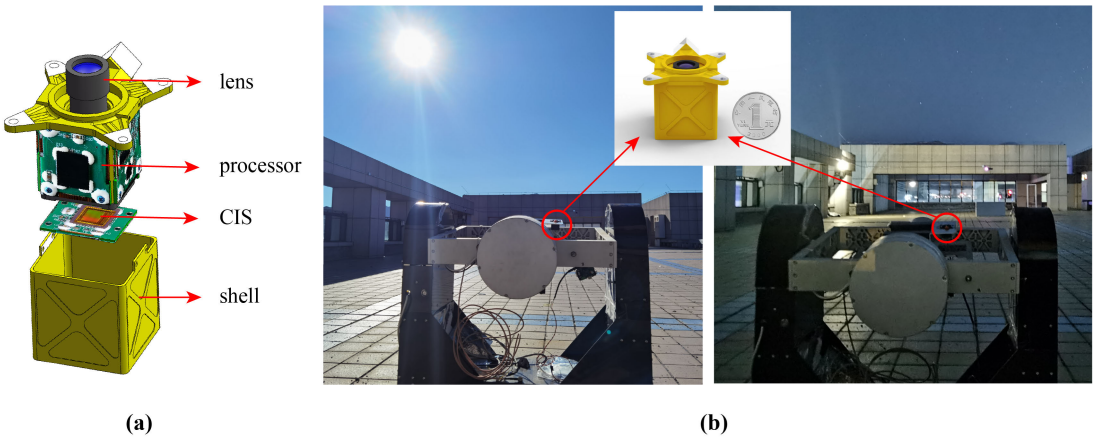

Fig. 6. Instrument model and experiment setup. (a) Three-dimensional model drawing of the designed all-day optical attitude sensor. (b) Sun observation and star observation experiment equipment and scenes.

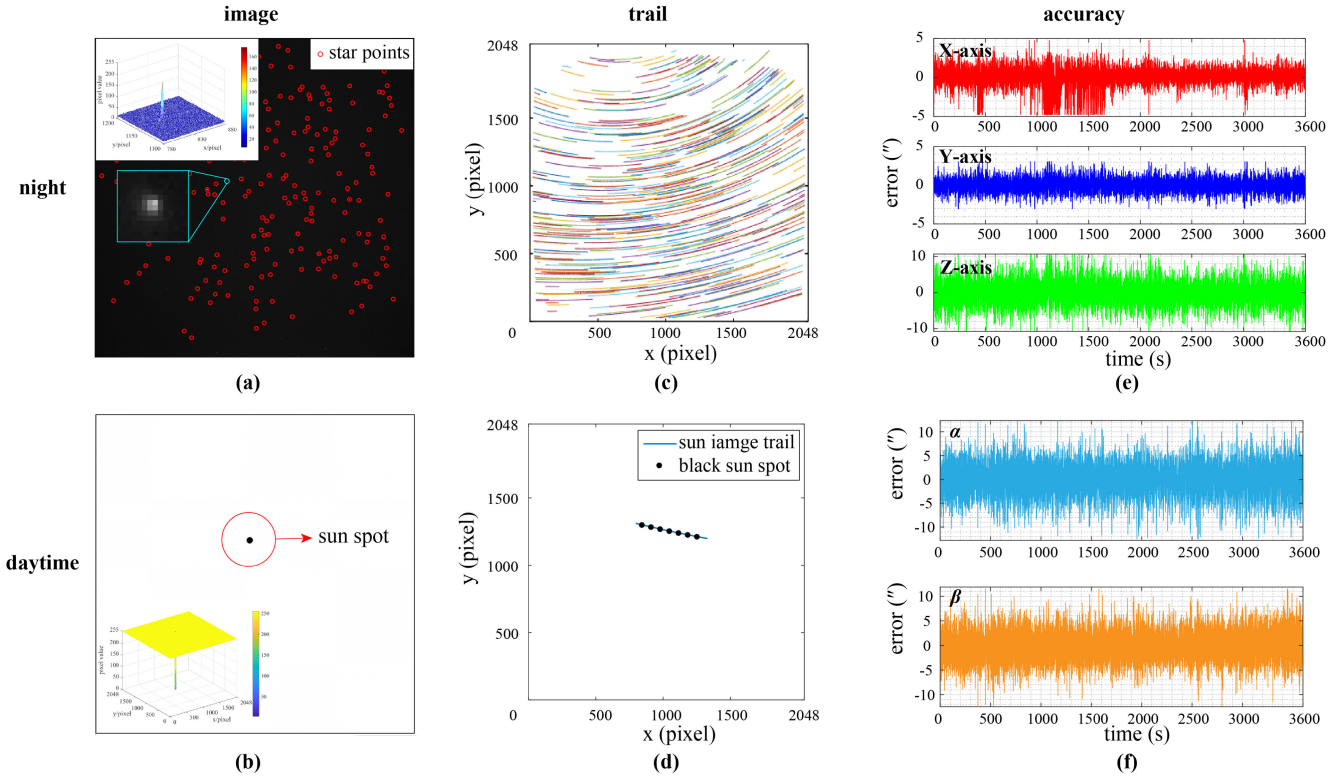

Fig. 7. Experiment results of the all-day attitude sensor. (a) Star observation image with identified star points marked. The pixel value distribution of one of the star points is shown in the upper left corner. (b) Sun observation image. The pixel value distribution is shown in the upper left corner. (c) Star trails of the identified star points. (d) Sun image trail with the black sun spot indicated at every 2000 frames. (e) Errors (3σ) of the three-axis attitude measured by the attitude sensor. (f) Errors (3σ) of the two-axis solar incidence angle measured by the attitude sensor.

56° and a theoretical angle measurement precision of 10.7" according to (9) and (10). The 3-D model of the attitude sensor can be seen in Fig. 6(a). It was manufactured and calibrated in the laboratory. The parameters of the integrated all-day optical attitude sensor are shown in the Table II.

In order to verify the feasibility and measurement accuracy of the integrated optical attitude sensor, ground-based star and sun observation experiments were carried out. The experiment setup is shown in Fig. 6(b). The sensor is fixed and kept stable to image the starry sky or the sun. As the earth rotates, the position of each star point or the sun image moves, and the update rate is 10 Hz. The three-axis attitude when it works as a star sensor and the two-axis solar incidence angle when it works as a sun sensor are measured.

The star observation experiment was carried out outdoors on a sunny night. The orientation of the sensor was adjusted to point to the zenith. The exposure time is 100 ms, and the PGA gain is set as 10. Consecutive 36 000 frames of images were sampled. One of the star images is shown in Fig. 7(a). The star trails of the identified star points are shown in Fig. 7(c). The errors are shown in Fig. 7(e). The results of the experiment are analyzed, and the X-axis (pitch), Y-axis (yaw) and Z-axis (roll) are 4.76" (3σ), 3.05" (3σ) and 10.72" (3σ), respectively.

In order to avoid the sun being blocked by surrounding buildings, the sun observation experiment was carried out outdoors at noon on a sunny day, and the orientation of the integrated attitude sensor was adjusted so that the sun was in the FOV. The exposure time is 10 ms, and the PGA gain is set as 10. Similarly, consecutive 36 000 frames of images were sampled. One of the images is shown in Fig. 7(b). It should be explained here that the reason why Fig. 7(b) is different from Fig. 4(b) is that the instrument used to take the latter is equipped with a neutral filter, so the number of photons arriving at the image sensor is attenuated, and the background light intensity is not enough to saturate all pixels, and the pixels far from the sun center are still working with the linear response. The sun image trail is shown in Fig. 7(d), and the black sun spot is indicated at every 2000 frames. The angle measurement errors are shown in Fig. 7(f). The results of the experiment are analyzed, and the X-axis and Y-axis errors are 8.42" (3σ) and 7.36" (3σ), respectively.

The real sky observation experiments verify the effectiveness and applicability of the proposed extended pixel response model of CIS. They also verify that the developed sensor successfully integrates the functions of sun sensors and star sensors, and achieves all-day attitude measurement with high accuracy of arcseconds level. Through detailed analysis and optimized design, the accuracy of the sun measurement has been significantly improved compared with the existing camera-based sun sensors, while maintaining the high-precision star measurement function.

V. Discussion and Conclusion

A. Discussion and Conclusion

The work of this article is based on the CMOS active-pixel sensor (APS) image sensor with 4T-PPD pixels and a CDS readout circuit. The general principle of pixel signal generation and readout is analyzed. The pixel readout value is obtained by subtracting the signal level and the reset level. Considering that the ability of the pixel to collect and accumulate photoelectrons is limited, when the pixels are exposed to extremely strong light, the excess electron generated may overflow and raise the reset sampling level by mistake, if there is no compensation. In this case, the pixel value decreases from the saturated value. Given this, the extended CIS pixel response model is established. In addition to the linear and saturation stages, the oversaturation stage is considered, which can respond to extremely strong light. It greatly extends the light intensity response range of CIS pixels and opens up a measurement pattern of full-range light intensity imaging.

Based on this, we can innovatively realize the integration of the star sensor and the sun sensor, that is, a single camera can image the stars as bright spots while imaging the sun as a black spot. The black spot of the sun image can be easily extracted, avoiding the influence of artifacts with irregular shapes, and thereby the accuracy of the solar incidence angle measurement is improved. Based on the detailed principle analysis, the feasible design method of the optical system is described in the article. Through ground-based sun and stars observation experiments, the feasibility of the integrated optical attitude sensor is verified, and the accuracy is demonstrated. Results show that the orientation accuracy from sun measurement is better than 9" (3σ), and the attitude accuracy from star measurement is better than 5" (3σ) for pointing and 11" (3σ) for rolling respectively. Existing conventional sun sensors have the highest accuracy up to about 0.01° [44]. It can be seen that while maintaining the high-precision stars measurement function, the integrated sensor also has the ability to measure the sun in the daytime, and the accuracy is significantly better than the existing camera-based sun sensors. Without increasing the complexity of the system and algorithm, a double-function and high-performance measurement instrument is realized.

Besides, considering the design of the sun sensor, the FOV of the all-day sensor is larger than that of typical star sensors, and therefore the number of identified stars in the FOV increases, which improves the accuracy under the condition of poorer angular resolution. In addition, it does not need a baffle to eliminate sunlight interference when applied to the land or aviation at night, reducing the mass and volume compared with typical star sensors in space.

Since the pixel charge overflow is a very complicated process, which is related to the design of the CIS pixel array semiconductor structure, this article makes some approximations to the modeling of the pixel oversaturation response stage. The actual effect can be confirmed by experiments.

B. Potential Applications

Based on the conventional pixel response model, the image sensor can only respond effectively to photoelectrons that do not exceed FWC, and the pixel response range of light intensity is limited. This work extends the pixel response model based on the analysis of the pixel signal generation and readout, proposes the extended response model for the extremely different light intensity range, and establishes a new celestial measurement pattern, which is a progress in the measurement field.

The integrated optical attitude sensor has the characteristics of both double-function and miniaturization, which provides possible solutions for high-precision all-day celestial navigation systems. In space applications, when the sun is in the FOV and the image is suffered from crosstalk phenomena such as blooming, leading the star sensor to face failure, the all-day sensor can continue to work as a sun sensor. In the last century, celestial navigation has been applied to aircraft such as long-range bombers, large transport aircraft, and reconnaissance aircraft [45]. In recent decades, unmanned aerial vehicles (UAVs) are increasingly developed and are used in a series of missions, including military and civil [46], [47]. The development of long-endurance UAVs is one of the focuses. They can work for a long time, even more than several days, and stay at the high altitude as pseudo-satellites, which can be used in a role similar to low-earth orbit satellites [48]. Zephyr and Solara are typical examples of high-altitude long endurance aircraft, and they work day and night. For small and micro UAVs, the all-day working ability is also important. At present, UAV navigation mainly depends on the inertial system and GPS. However, during

long-time flight, the accumulated error of inertial navigation cannot be ignored. Besides, because of huge advancements in technology, UAVs have a high probability of experiencing attacks such as GPS spoofing [49]. Celestial and inertial integrated navigation system applied to UAVs is a topic of interest, which is a good alternative to GPS [50]. At present, celestial navigation is mainly based on star sensors [14], [51]. There are also researchers who deploy the sun sensor or the polarization sensor on quadrotor UAVs to coordinate with inertial sensors to achieve navigation [20], [24]. The proposed all-day attitude sensor can provide a reliable and high-precision navigation sensor for UAVs, making them capable of long-endurance flying and working day and night. Besides, miniaturization is also an important development trend of UAVs. Weight and size are significant considerations of the payload design [52], [53]. Therefore, lightweight and small-size are also important advantages for the proposed sensors to be selected.

In UAV navigation applications, the proposed all-day optical attitude sensor can be combined with the miniature inertial measurement unit (MIMU) to achieve localization, which will be the follow-up research. The attitude provided by the stars measurement of the integrated sensor can be combined with the MIMU to realize night navigation. While during the daytime, navigation can be achieved by combining the sun vector at different sampling moments provided by the sun measurement with the MIMU. It solves the problem that it is difficult for the daytime star sensor to identify a sufficient number of stars during the day and the high-precision daytime star sensors usually have a large mass and volume. Besides, compared with the typical star sensors with a baffle used in space, the all-day sensors applied to UAVs do not need a baffle to eliminate the sunlight interference when working as a star sensor during the night.

REFERENCES

[1] M. Sadraey, "Navigation system design," in *Unmanned Aircraft Design: A Review of Fundamentals*. San Rafael, CA, USA: Morgan & Claypool, 2017, ch. 5, pp. 91–97.

[2] W. Truszkowski, H. L. Hallock, C. Rouff, J. Karlin, J. Rash, and M. Hinchey, *Autonomous and Autonomic Systems: With Applications to NASA Intelligent Spacecraft Operations and Exploration Systems*. Cham, Switzerland: Springer, 2009.

[3] T. Glotzbach, *Navigation of Autonomous Marine Robots: Novel Approaches Using Cooperating Teams*. Cham, Switzerland: Springer, 2020.

[4] D. M. Rakovic, A. Simonovic, and A. M. Grbovic, "UAV positioning and navigation—Review," in *Proc. CNNTech*, Zlatibor, Serbia, 2021, pp. 220–256.

[5] H. Umland. (2019). *A Short Guide to Celestial Navigation*. [Online]. Available: https://www.celnav.de/astro.zip

[6] F. Pappalardi, S. J. Dunham, M. E. LeBlang, T. E. Jones, J. Bangert, and G. Kaplan, "Alternatives to GPS," in *Proc. MTS/IEEE Oceans Ocean Odyssey Conf.*, Nov. 2001, pp. 1452–1459.

[7] R. Strydom, A. Denuelle, and M. V. J. A. Srinivasan, "Bio-inspired principles applied to the guidance, navigation and control of UAS," *Aerospace*, vol. 3, no. 21, pp. 1–34, 2016.

[8] M. Ahmad, M. A. Farid, S. Ahmed, K. Saeed, M. Asharf, and U. Akhtar, "Impact and detection of GPS spoofing and countermeasures against spoofing," in *Proc. 2nd Int. Conf. Comput., Math. Eng. Technol. (iCoMET)*, Jan. 2019, pp. 1–8.

[9] J. Ali, C. Zhang, and J. Fang, "An algorithm for astro-inertial navigation using CCD star sensors," *Aerosp. Sci. Technol.*, vol. 10, no. 5, pp. 449–454, Jul. 2006.

[10] C. Zhang et al., "A lightweight and drift-free fusion strategy for drone autonomous and safe navigation," *Drones*, vol. 7, no. 1, p. 34, Jan. 2023.

[11] H.-Y. Lin and J.-R. Zhan, "GNSS-denied UAV indoor navigation with UWB incorporated visual inertial odometry," *Measurement*, vol. 206, Jan. 2023, Art. no. 112256.

[12] X. Ning, M. Gui, Y. Xu, X. Bai, and J. Fang, "INS/VNS/CNS integrated navigation method for planetary rovers," *Aerosp. Sci. Technol.*, vol. 48, pp. 102–114, Jan. 2016.

[13] B. Gou and Y.-M. Cheng, "INS/CNS integrated navigation based on corrected infrared Earth measurement," *IEEE Trans. Instrum. Meas.*, vol. 68, no. 9, pp. 3358–3366, Sep. 2019.

[14] N. Xiaolin, Y. Weiping, and L. Yanhong, "A tightly coupled rotational SINS/CNS integrated navigation method for aircraft," *J. Syst. Eng. Electron.*, vol. 30, no. 4, pp. 770–782, Aug. 2019.

[15] J. Bao, H. Zhan, T. Sun, S. Fu, F. Xing, and Z. You, "A window-adaptive centroiding method based on energy iteration for spot target localization," *IEEE Trans. Instrum. Meas.*, vol. 71, pp. 1–13, 2022.

[16] J. Yang, J. Jiang, L. Tian, and G. Zhang, "Joint estimation of stellar atmospheric refraction and star tracker attitude," *IEEE Trans. Instrum. Meas.*, vol. 71, pp. 1–12, 2022.

[17] Z. Ma, H. Wang, Y. Shen, Y. Xue, and H. Yan, "Design of hybrid refractive-diffractive star sensor optical system with wide field and small F-number," *Proc. SPIE*, vol. 12069, pp. 204–209, Nov. 2021.

[18] E. J. Knobbe and G. N. Haas, "Celestial navigation," in *Avionics Navigation Systems*. Hoboken, NJ, USA: Wiley, 1997, pp. 551–596.

[19] X. Zheng, Y. Huang, X. Mao, F. He, and Z. Ye, "Research status and key technologies of all-day star sensor," in *Proc. 10th ACMAE*, Bangkok, Thailand, 2019, pp. 1–7.

[20] S. Jung, C. Liu, and K. B. Ariyur, "Absolute orientation for a UAV using celestial objects," in *Proc. AIAA Infotech@Aerospace (I@A) Conf.*, Aug. 2013, pp. 1–12.

[21] J. Barnes, C. Liu, and K. Ariyur, "A hemispherical sun sensor for orientation and geolocation," *IEEE Sensors J.*, vol. 14, no. 12, pp. 4423–4433, Dec. 2014.

[22] C. Liu, F. Yang, and K. B. Ariyur, "Interval-based celestial geolocation using a camera array," *IEEE Sensors J.*, vol. 16, no. 15, pp. 5964–5973, Aug. 2016.

[23] J. Chahl and A. Mizutani, "Biomimetic attitude and orientation sensors," *IEEE Sensors J.*, vol. 12, no. 2, pp. 289–297, Feb. 2012.

[24] J. Yang, T, Du, X. Liu, B. Niu, and L. Guo, "Method and implementation of a bioinspired polarization-based attitude and heading reference system by integration of polarization compass and inertial sensors," *IEEE Trans. Ind. Electron.*, vol. 67, no. 11, pp. 9802–9812, Nov. 2020.

[25] L. Guan, S. Li, L. Zhai, S. Liu, and H. Xie, "Study on skylight polarization patterns over the ocean for polarized light navigation application," *Appl. Opt.*, vol. 57, no. 21, pp. 6243–6251, 2018.

[26] Q. Zhang, J. Yang, X. Liu, and L. Guo, "A bio-inspired navigation strategy fused polarized skylight and starlight for unmanned aerial vehicles," *IEEE Access*, vol. 8, pp. 83177–83188, 2020.

[27] L. Zhang, H. Zhan, X. Liu, F. Xing, and Z. You, "A wide-field and high-resolution lensless compound eye microsystem for real-time target motion perception," *Microsyst. Nanoeng.*, vol. 8, no. 1, p. 83, Jul. 2022.

[28] M. Wei, F. Xing, Z. You, and G. Wang, "Multiplexing image detector method for digital sun sensors with arc-second class accuracy and large FOV," *Opt. Exp.*, vol. 22, no. 19, pp. 23094–23107, Sep. 2014.

[29] K. Bolshakov, F. K. Diriker, R. Clark, R. Lee, and H. Podmore, "Array-based digital sun-sensor design for CubeSat application," *Acta Astronautica*, vol. 178, pp. 81–88, Jan. 2021.

[30] A. Trebi-Ollennu, T. Huntsberger, Y. Cheng, E. T. Baumgartner, B. Kennedy, and P. Schenker, "Design and analysis of a sun sensor for planetary rover absolute heading detection," *IEEE Trans. Robot. Autom.*, vol. 17, no. 6, pp. 939–947, Dec. 2001.

[31] P. V. Hough, "Method and means for recognizing complex patterns," U.S. Patent 3 069 654, Dec. 18, 1962.

[32] R. Saleem, S. Lee, and J. Kim, "A cost-effective micro sun sensor based on black sun effect," in *Proc. IEEE Sensors*, Oct. 2017, pp. 1470–1472.

[33] R. Saleem and S. Lee, "Accurate and cost-effective micro sun sensor based on CMOS black sun effect," *Sensors*, vol. 19, no. 3, p. 739, Feb. 2019.

[34] H.-J. Kim, "A sun-tracking CMOS image sensor with black-sun readout scheme," *IEEE Trans. Electron Devices*, vol. 68, no. 3, pp. 1115–1120, Mar. 2021.

[35] M. Belenkii, D. Bruns, V. Rye, and T. Brinkley, "Daytime stellar imager," U.S. Patent 7 349 804, Mar. 25, 2008.

[36] E. R. Fossum and D. B. Hondongwa, "A review of the pinned photodiode for CCD and CMOS image sensors," *IEEE J. Electron Devices Soc.*, vol. 2, no. 3, pp. 33–43, May 2014.
[37] J. Ohta, "Fundamentals of CMOS image sensors," in *Smart CMOS Image Sensors and Applications*, 2nd ed. Boca Raton, FL, USA: CRC Press, 2020, pp. 40–42.
[38] M. Sarkar, B. Büttgen, and A. J. P. Theuwissen, "Feedforward effect in standard CMOS pinned photodiodes," *IEEE Trans. Electron Devices*, vol. 60, no. 3, pp. 1154–1161, Mar. 2013.
[39] J. Nakamura, "Basics of image sensors," in *Image Sensors and Signal Processing for Digital Still Cameras*. Boca Raton, FL, USA: CRC Press, 2006, pp. 59–60.
[40] U. Khan and M. Sarkar, "Analysis of charge transfer potential barrier in pinned photodiode of CMOS image sensors," *IEEE Trans. Electron Devices*, vol. 68, no. 6, pp. 2770–2777, Jun. 2021.
[41] M. Khabir, H. Alaibakhsh, and M. A. Karami, "Electrical crosstalk analysis in a pinned photodiode CMOS image sensor array," *Appl. Opt.*, vol. 60, no. 31, pp. 9640–9650, Nov. 2021.
[42] *European Machine Vision Association, Release 3.1, EMVA*, Standard EMVA 1288, Standard for Characterization of Image Sensors and Cameras, 2016. [Online]. Available: https://www.emva.org/wp-content/uploads/EMVA1288-3.1a.pdf
[43] C. C. Liebe, "Accuracy performance of star trackers—A tutorial," *IEEE Trans. Aerosp. Electron. Syst.*, vol. 38, no. 2, pp. 587–599, Apr. 2002.
[44] Q. Zhang and Y. Zhang, "Design and verification of an integrated panoramic sun sensor atop a small spherical satellite," *Sensors*, vol. 22, no. 21, p. 8130, Oct. 2022.
[45] X. Wang, H. Zhang, and X. Gao, "Overview of the INS/CNS integrated navigation technology," *Proc. SPIE*, vol. 10843, Feb. 2019, Art. no. 1084303.
[46] J.-P. Condomines, "Introduction to aerial robotics," in *Nonlinear Kalman Filter for Multi-Sensor Navigation of Unmanned Aerial Vehicles: Application to Guidance and Navigation of Unmanned Aerial Vehicles Flying in a Complex Environment*. Amsterdam, The Netherlands: Elsevier, 2018, ch. 1, pp. 1–5.
[47] K. K. Rumayshah, A. Prayoga, and M. A. Moelyadi, "Design of high altitude long endurance UAV: Structural analysis of composite wing using finite element method," *J. Phys., Conf. Ser.*, vol. 1005, Apr. 2018, Art. no. 012025, doi: 10.1088/1742-6596/1005/1/012025.
[48] A. Bakar, L. Ke, H. Liu, Z. Xu, and D. Wen, "Design of low altitude long endurance solar-powered UAV using genetic algorithm," *Aerospace*, vol. 8, no. 8, p. 228, Aug. 2021.
[49] G. E. M. Abro, S. A. B. M. Zulkifli, R. J. Masood, V. S. Asirvadam, and A. Laouti, "Comprehensive review of UAV detection, security, and communication advancements to prevent threats," *Drones*, vol. 6, no. 10, p. 284, Oct. 2022.
[50] S. Teague and J. Chahl, "Imagery synthesis for drone celestial navigation simulation," *Drones*, vol. 6, no. 8, p. 207, Aug. 2022.
[51] F. Ting and X. Huang, "Inertial/celestial integrated navigation algorithm for long endurance unmanned aerial vehicle," *Acta Tech.*, vol. 62, no. 2B, pp. 205–217, Aug. 2017.
[52] M. Logan, J. Chu, M. Motter, D. Carter, M. Ol, and C. Zeune, "Small UAV research and evolution in long endurance electric powered vehicles," in *Proc. AIAA Infotech@Aerospace Conf. Exhib.*, May 2007, p. 2730.
[53] J. Everaerts, N. Lewyckyj, and D. Fransaer, "Pegasus: Design of a stratospheric long endurance UAV system for remote sensing," *Int. Arch. Photogramm., Remote Sens. Spatial Inf. Sci.*, vol. 35, pp. 29–33, Jul. 2004.

Hongjing Cao was born in 1998. She received the B.S. degree in measurement and control technology and instrument from the School of Precision Instrument and Opto-electronics Engineering, Tianjin University, Tianjin, China, in 2020. She is currently pursuing the Ph.D. degree with the Department of Precision Instrument, Tsinghua University, Beijing, China.

Her research interests include high-precision optical measurements.

Haiyang Zhan was born in 1996. He received the B.S. degree in automation from the Beijing Institute of Technology, Beijing, China, in 2017. He is currently pursuing the Ph.D. degree with the Department of Precision Instrument, Tsinghua University, Beijing.

His research interests include high-precision optical measurements.

Jingdong Li was born in 1994. He received the B.S. degree in communication engineering from the Beijing University of Posts and Telecommunications, Beijing, China, in 2016, and the M.S. degree from Tsinghua University, Beijing, in 2019.

After graduation, he joined China Telecom, Beijing, as a Senior Software Engineer. His research interests include high-precision optical measurements.

Qilong Rao received the B.S. degree from the Nanjing University of Aeronautics and Astronautics, Nanjing, China, in 2005, and the M.S. degrees in electronic and communication engineering from Shanghai Jiaotong University, Shanghai, China, in 2012.

After graduation, he devoted himself to the overall design of optical remote-sensing satellites. In 2015, he obtained the title of senior engineer.

Mr. Rao was won the Third Prize of Shanghai Science and Technology Progress Award in 2012.

Fei Xing received the B.S. degree in mechanical engineering from Tongji University, Shanghai, China, in 2002, and the Ph.D. degree from Tsinghua University, Beijing, China, in 2006.

After graduation, he joined the Department of Precision Instrument, Tsinghua University, as an Assistant Researcher. He was a Yangtze River Scholar Award Program Professor in 2020. He became a Professor in 2021. He has published more than 70 articles. His main research interest includes micro-miniature high-precision attitude measurement sensor technology.

Dr. Xing was awarded the Xplorer Prize in 2021.

Zheng You received the B.S., M.S., and Ph.D. degrees from the Huazhong University of Science and Technology, Wuhan, China, in 1985, 1987, and 1990, respectively.

After graduation, he joined the Department of Precision Instrument, Tsinghua University, Beijing, China, as an Assistant Professor. He became an Associate Professor in 1992 and a Full Professor in 1994. In 2015, he was the Vice President of Tsinghua University. He was a Yangtze River Scholar Award Program Professor in 2001, and an Academician by the Chinese Academy of Engineering in 2013. He has published more than 400 articles. His main research interests include micro-nano technology and micro-nano satellite technology.